Materials Advances

ROYAL SOCIETY OF CHEMISTRY

COMMUNICATION

View Article Online
View Journal | View Issue

Cite this: *Mater. Adv.*, 2023, 4, 2410

Received 8th March 2023,
Accepted 15th May 2023

DOI: 10.1039/d3ma00068k

rsc.li/materials-advances

A fluorescent sensor to detect lead leakage from perovskite solar cells†

Lorenzo Pancini, Riccardo Montecucco, Valentina Larini, Alessandra Benassi, Diego Mirani, Giovanni Pica, Michele De Bastiani, Filippo Doria * and Giulia Grancini *

Hybrid perovskites have been considered a hot material in the semiconductor industry; included as an active layer in advanced devices, from light emitting applications to solar cells, where they lead as a new strategic solution, they promise to be the next generation high impact class of materials. However, the presence – in most cases – of lead in their matrix, or lead byproducts as a consequence of material degradation, such as PbI_2, is currently hindering their massive deployment. Here, we develop a fluorescent organic sensor (FS) based on the Pb-selective BODIPY fluorophore that emits when the analyte – lead in this case – is detected. We carried out a fluorimetric analysis to quantify the trace concentration of Pb^{2+} released from lead-based perovskite solar cells, exploring different material compositions. In particular, we immersed the devices in rainwater, to simulate the behavior of the devices under atmospheric conditions when the sealing is damaged. The sensor is studied in a phosphate buffer solution (PBS) at pH 4.5 to simulate the pH of acidic rain, and the results obtained are compared with ICP-OES measurements. We found that with fluorometric analysis, lead concentration could be calculated with a detection limit as low as 5 μg l^{-1}, in agreement with ICP-OES analysis. In addition, we investigated the possibility of using the sensor on a solid substrate for direct visualization to determine the presence of Pb. This can constitute the base for the development of a Pb-based label that can switch on if lead is detected, alerting any possible leakage.

1. Introduction

Perovskite solar cells (PSCs) are an emerging photovoltaic technology and show great promise to disrupt the solar cell market. Indeed, in less than ten years, PSCs have achieved record power conversion efficiencies (PCE) of 25.7%[1] close to those of the most efficient crystalline silicon technologies.[2] These remarkable achievements are due to the unique optoelectronic properties of PSCs, such as the defect tolerance, steep absorption coefficient,[3] long diffusion length,[4] and tunable bandgap.[5] Nowadays, the most efficient formulation of PSCs always includes lead as the B-site divalent-cation[6] in the ABX_3 structure[7] (Fig. 1(a)).

Despite their excellent properties these devices suffer from poor stability under environmental conditions: hybrid perovskites tend to degrade in the presence of heat[8] and moisture[9] and upon exposure to light and oxygen[10] releasing several byproducts including PbI_2. High humidity conditions promote the formation of the hydrated complex with the perovskite causing structural deformation and the release of PbI_2,[11] as shown in the XRD diffraction pattern in Fig. 1(b), obtained by recording the XRD measurements of the $MAPbI_3$ perovskite at different times and under RH 75% conditions. The XRD pattern after 24 hours shows the degradation of the perovskite: the peaks related to PbI_2 are assigned to the (001), (100) and (003) planes at angles 12.76°, 22.07° and 38.69°, respectively. The diffraction peaks at 14.20°, 20.04°, 23.56°, 24.58°, 28.52° and 31.95° related to $MAPbI_3$ correspond to the planes (110), (200), (211), (202), (220) and (310). In addition, the organic cation can further degrade, causing the release of additional byproducts including HI and methylamine,[12] as shown in eqn (1).

$$(CH_3NH_3)_4PbI_6{\cdot}2H_2O \rightarrow PbI_2 + 4CH_3NH_2 + 4HI + 2H_2O \quad (1)$$

Perovskite solar cells are unstable even under prolonged thermal stress. At 40 °C, which is the typical temperature reached by solar modules under the operating conditions, the perovskite is subjected to the degradation pathway that leads to the initial precursors according to eqn (2). By increasing the temperature, the decomposition of the organic cation also occurs with the release of volatile compounds.[13]

$$CH_3NH_3PbI_3 \; CH_3NH_3I + PbI_2 \quad (2)$$

Moreover, exposure to light and oxygen are other key factors in the stability of perovskites. Molecular oxygen can be adsorbed

Department of Chemistry & INSTM Università di Pavia, Via T. Taramelli 14, Pavia 27100, Italy. E-mail: filippo.doria@unipv.it, giulia.grancini@unipv.it

† Electronic supplementary information (ESI) available. See DOI: https://doi.org/10.1039/d3ma00068k

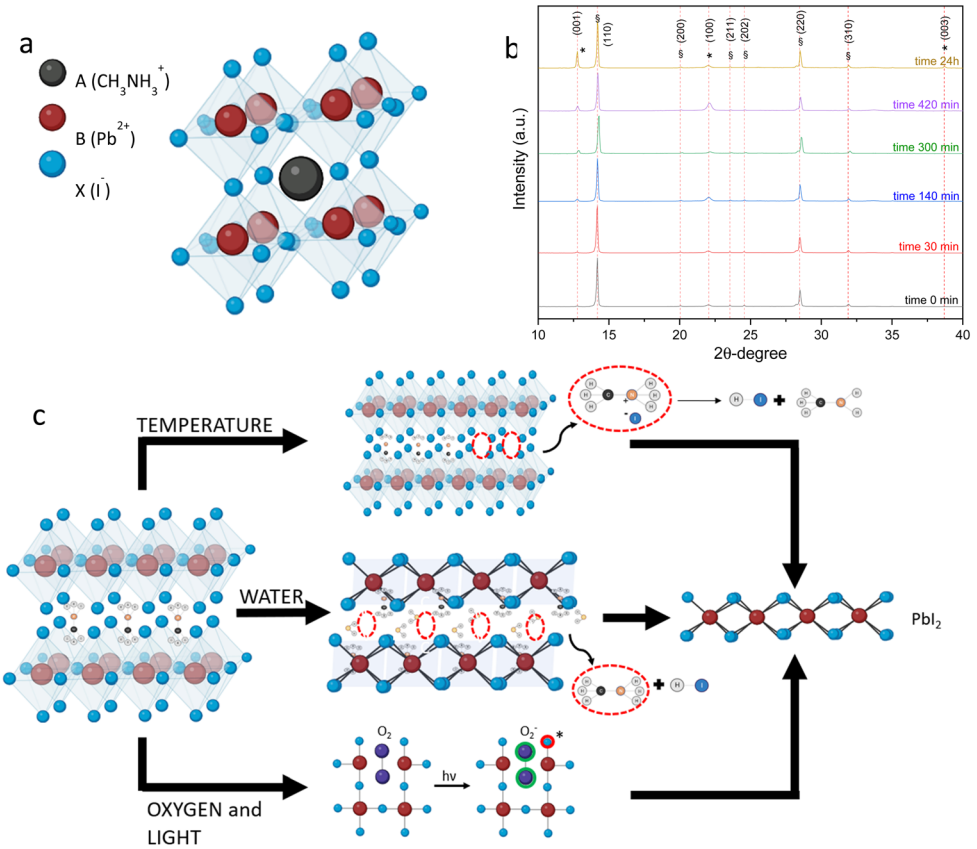

Fig. 1 Generic crystal structure of an organic–inorganic hybrid perovskite where A is the organic cation, B is the inorganic cation and X is the anion, usually halogen (a); XRD patterns of the $MAPbI_3$ perovskite stored under high humidity conditions (RH 75%), at different times (b); a schematic representation of the different degradation pathways and byproducts released by the $MAPbI_3$ perovskite (c).

and then reversibly diffused through the iodide vacancies. Upon photoexcitation, perovskite reacts with the superoxide species O_2^-, which initiates an acid–base reaction with the MA^+ cation through deprotonation, forming water molecules, iodine, lead iodide, and methylamine gas,[14] as shown in eqn (3).

$$4CH_3NH_3PbI_3^* + O_2^- \rightarrow 4PbI_2 + 2H_2O + 4CH_3NH_2 + 2I_2 \quad (3)$$

Most of the byproducts generated by these different degradation pathways (summarized in Fig. 1(c)) are remarkably dangerous, due to lead toxicity in an aqueous environment and towards living organisms.[15]

For this reason, several attempts have been made to replace the Pb cation. Among these attempts, double perovskites based on Ag and Bi[16] were identified as possible candidates, but unfortunately, their maximum photovoltaic performances of 4.3% are not sufficiently high. Replacing Pb with Sn is possible and the theoretical PCE limit for Sn-based PSCs is 30%;[17] the main issue with tin-based perovskite cells is instability due to the tendency of Sn^{2+} to oxidize to Sn^{4+}. However, tin is used to fabricate Sn–Pb based perovskites, in which lead is partially replaced. This allows the production of more high-performance and tunable band gap devices.[18] In addition to single junction perovskite cells, hybrid Sn–Pb perovskites have found great application as low-band gap perovskite sub-cells for tandem devices.[19–21] Therefore, it is very likely that PSCs will seek their early commercialization with Pb-based formulation. This translates into higher manufacturing costs due to the extra caution required for the production process and waste management. Moreover, it will be necessary to secure any potential environmental contamination from the perovskite modules once degraded outdoors. The lead once released as a by-product from the perovskite modules presents a serious hazard.[22] Lead, being a heavy metal, can contaminate the soil and then can be bioaccumulated by plants, becoming a threat to other living organisms. In addition, lead in the form of PbI_2 is much more easily adsorbed by plants[23] than all other sources of lead in the soil. For human beings, the main hazard of lead poisoning is related to its ability to penetrate soft tissues and replace the metal cations in our bodies by interfering with major enzyme functions. Exposure to high concentrations of the lead causes anemia, increased blood pressure, neurodegenerative diseases,[24] and even death.[25]

Motivated by these reasons, we developed a chemical sensor, selective for Pb^{2+}, that is able to detect the presence of Pb^{2+} in liquids with a limit of detection (LOD) of 5.23 μg l^{-1}. The sensor has intrinsic fluorescence quenched by the process of photo-induced electron transfer (PET) in which the lone pair of nitrogen atoms are involved. In the presence of the lead cation, complexation occurs with the nitrogen of the aromatic core and

side chains. This complexation prevents PET and allows the relative enhancement of the photoluminescence, as investigated in ref. 26 but is never applied to the detection of Pb-leaks caused by PSCs. In recent years various techniques have been developed for the detection of lead analytes. Guo *et al.* have developed an amino-functionalized Ni(II)-based metal–organic framework (MOF)[27] capable of selectively detecting trace amounts of Pb^{2+} through square wave anodic stripping voltammetry (SWASV) analysis. Marawani *et al.* have synthesized carboxyl-functionalized multiwall carbon nanotubes (f-MWCNTs)[28] capable of selectively detecting lead in an aqueous solution through ICP-OES analysis with an uptake capacity of 72.12 mg g^{-1} and a detection limit of 0.25 ng l^{-1}. Another work, based on the ICP-OES technique, was reported by Smirnova *et al.*[29] The total lead concentration was measured through a pre-concentration process in a two-phase aqueous system of tetrabutylammonium bromide (TBAB)–H_2O–$(NH_4)_2SO_4$ and extraction with 4-(2-pyridylazo)-resorcinol. The extract was captured with an oleophilic collector and analyzed with ICP-OES, showing a LOD of 0.2 μg l^{-1}. Song *et al.* reported in their recent work an analytical method based on HPLC-ICP-MS instrument capable of detecting Pb^{2+} traces in different aqueous sources: drinking water, river water, pond water, and tap water.[30] The LOD of the developed method is 0.004 ηg L^{-1}, well below the legal limits, and with a linear range between 0.1 and 100 ηg L^{-1}. Another approach for lead detection is the study conducted by Yu *et al.* in which lignin-functionalized Au NPs (L-Au NPs) are used.[31] The color change of L-Au NPs from red to purple indicates the presence of Pb^{2+} ions. This technique allows for the detection of Pb even at low concentrations (LOD of 1.8 μM) in a linear range of 0.1–1 mM. Finally, Aamir *et al.* reported a cesium-based perovskite sensor capable of selectively detecting Pb^{2+}.[32] In the presence of the cations Cr^{3+}, Co^{2+}, Cd^{2+}, Fe^{2+}, Mn^{2+}, and Zn^{2+}, the photoluminescence response of the $CsCuCl_3$ perovskite in the presence of Pb^{2+} remains almost unchanged. Furthermore, they observed that the linear range goes from 0.1 μM to 1.5 μM, demonstrating that it can be used as a turn-on sensor for detecting Pb^{2+}.

The sensors reported in the literature are valid alternatives to the FS proposed in this work. However, the main advantages of our sensor are the low cost and velocity of the fluorescence technique, the ability to detect and quantify Pb, and the small amount of time required for the sample preparation and measurement. Techniques based on ICP have better LOD and sensitivity, but the high cost of equipment and the need for sample pre-treatment makes them less suitable for practical applications where quick detection is required. A $CsCuCl_3$-based perovskite is a very interesting inorganic sensor; however, the PL response of the sensor with Pb^{2+} may vary depending on the presence of Hg^{2+}. Finally, the colorimetric technique based on NPs has a linear range of 0.1–1 mM, which is too high compared to international standards. Additionally, the sensor's absorption signal varies over time due to NP aggregation.

Here, we investigate the detection properties of FS by dissolving PSCs of different compositions in ambient acid rain to mimic the leakage of a degraded module. We investigated the possibility of detecting Pb in the concentration range of 0 to 2.3 μM (476 μg l^{-1}) considering that the legal limits of Pb concentration for potable water are 10 μg l^{-1} according to World Health Organization (WHO) guidelines, 15 μg l^{-1} per the United States Environmental Protection Agency (USEPA)[33] and 10 μg l^{-1} per European Union (EU) Drink Water Directive (DWD).[34] We compared our results with measurements by ICP-OES to confirm the analytical data. The use of the organic sensor makes it possible to estimate $[Pb^{2+}]$ with accuracy by fluorimetric analysis, which has a significantly lower cost than the normal techniques used for metal detection such as ICP-OES and AAS. Lastly, we engineered our sensor in the solid-state, as a proof of concept for an early application.

2. Experimental section materials/methods

2.1 Materials

Competition study. Titanium(IV) diisopropoxide bis(acetylacetonate) (75% in isopropyl alcohol), bis(trifluoromethane) sulfonamide lithium salt (LiTFSI > 98.0%), potassium bromide (KBr > 99.0%), lead(II) iodide (PbI_2 > 99.99%), lead(II) chloride ($PbCl_2$ > 99.0%), lead(II) bromide ($PbBr_2$ > 98.0%), and cesium iodide (CsI, > 99.99%) were purchased from TCI. tin(II) chloride ($SnCl_2$ > 98.0%) and rubidium iodide (RbI, >99.99%) were purchased from Sigma Aldrich. Methylammonium iodide (MAI > 99.99%) and formamidinium iodide (FAI > 99.99%) were purchased from GreatCell Solar Materials.

$FAPbI_3$ perovskite materials. Chlorobenzene (CB, extra dry, 99.8%), dimethyl sulfoxide (DMSO, ≥99.9% extra dry) and *N*,*N*-dimethylformamide (DMF, 99.8%, extra dry) were purchased from Acros Organics. Tin(IV) oxide (SnO_2 15% in H_2O) was purchased from Alfa Aesar. Acetone (≥99.8%), 2-propanol (IPA, ≥99.8%), N^2,N^2,$N^{2'}$,$N^{2'}$, N^7,N^7,$N^{7'}$,$N^{7'}$-octakis(4-methoxyphenyl)-9,9′-spirobi-[9*H*-fluorene]-2,2′,7,7′-tetramine (Spiro-OMeTAD, 99%, HPLC), bis(trifluoromethane)sulfonimide lithium salt (Li–salt, 99.95%), acetonitrile (ACN, anhydrous, 99.8%), titanium(IV) diisopropoxide bis(acetylacetonate), dimethylammonium iodide (DMAI) and 4-*tert*-butylpyridine (4-*t*BP,98%) were purchased from Sigma-Aldrich. Lead iodide (PbI_2, >99.99%) and cesium iodide (CsI, >99.99%) were purchased from TCI. Formamidinium iodide (FAI, >99.99%), methylammonium chloride (MACl), 30NR-D titania and 4-methylphenethylammonium chloride (MePEACl) were purchased from GreatCell Solar Materials.

FS synthesis. 1,2-Phenylendiamine (99.5%), sodium iodide (NaI, ≥99.5%), diisopropylethylamine (DIPEA, 99.5%), ethyl bromoacetate, acetonitrile (CH_3CN, HPLC, ≥99.9%), dichloromethane (DCM, HPLC, ≥99.8%), cyclohexane (HPLC, ≥99.9%), ethyl acetate (≥99.5%), dry pyridine (anhydrous, 99.8%), dry DMF (anhydrous, 99.8%), phosphorous oxychloride (99.99%), sodium carbonate (99%), sodium sulfate (99%), 2,4-dimethylpyrrole (97%), trifluoroacetic acid (HPLC, 99%), 2,3-Dichloro-5,6-dicyano-*p*-benzoquinone (DDQ), BF_3–OEt_2 and diethanolamine (98%) were all purchased from Sigma Aldrich and used as received.

2.2 PSC fabrication

$FaPbI_3$ device. For the fabrication of PSCs, indium tin oxide (ITO)-coated glass substrates were consecutively cleaned in acetone and IPA by ultrasonicating for 15 min for each solvent. Substrates were dried with N_2 airflow and UV-ozone treated for 30 min. SnO_2 colloidal dispersion was diluted to 10% in water and 50 μL were spin-coated onto ITO/glass substrates and annealed at 150 °C for 30 min. Subsequently, SnO_2-coated substrates were subjected to UV-ozone treatment for 30 min. All solutions were prepared in an Ar-filled glovebox, while the deposition of each layer of the solar cell was performed in an N_2-filled glovebox. The perovskite precursor solution (1.2 M) was prepared by dissolving PbI_2 and FAI powders in a DMF/DMSO 4/1 solution with a 5% PbI_2 excess. For bulk treatment, 35 mol% of MACl was added to the solution. 25 μL of the final solution were deposited on the SnO_2-coated substrates and spin-coated using a three-step procedure: in the first step substrates were spun at 1000 rpm for 12 s, the second step proceeded at 5000 rpm for 27 s, while the last step was a speed reduction of 4 s. 10 s after the beginning of the second step, 150 μL of CB were dropped onto the spinning substrate for an antisolvent procedure. Subsequently, substrates were annealed at 150 °C for 30 min. For the surface passivation of the perovskite, 50 μL of a solution 0.01 M of MePEACl in IPA were spin-coated onto the perovskite layer at 4000 rpm for 30 s and substrates were annealed at 100 °C for 10 min. To fabricate the HTL, Spiro-OMeTAD was dissolved in CB to produce an 80 mg mL^{-1} solution. The solution was doped by adding 17.5 μL of Li salt dissolved in ACN (500 mg mL^{-1} in ACN) and 28.8 μL of 4-*t*BP to 1 mL of Spiro-OMeTAD solution in CB. 10 μL of the final solution were spin-coated onto the perovskite layer. Finally, 80 nm of Au were thermally evaporated on the device with a shadow mask of 0.0825 cm^2 area. The evaporation speed was adjusted to 0.01 nm s^{-1} for the first 5 nm, 0.02 nm s^{-1} from 5 to 15 nm, and 0.08 nm s^{-1} for the rest of the procedure.

$CsPbI_3$ device. Prepatterned FTO substrates (TEC 15) were sequentially cleaned with acetone and 2-propanol (IPA) by ultrasonication for 15 min in each solvent. The FTO/glass substrates were then dried with N_2 and treated with UV-Ozone cleaning for 15 min. The compact TiO_2 (c-TiO_2) layer was deposited on glass/FTO substrates by spray pyrolysis of a 1 : 15 (v : v) mixture of titanium(IV) diisopropoxide bis(acetylacetonate) and IPA at 450 °C, followed by an annealing at 450 °C for 1 h. Then, the mesoporous TiO_2 (m-TiO_2) was spin-coated from a 1 : 8 (m/v) mixture of 30NR-D titania paste and ethanol on top of the c-TiO_2. The spin coating program was 5000 rpm, 20 s, 2000 rpm. The substrates were then annealed at 500 °C for 20 minutes. The 0.85 $CsPbI_3$ perovskite precursor solution was prepared by dissolving stoichiometric CsI, PbI_2 and DMAI with a 1 : 1 : 1 molar ratio in a solvent mixture (DMF/DMSO = 4/1 vol : vol). Then, the $CsPbI_3$ active layer was spin-coated on top of the FTO/c-TiO_2/m-TiO_2 substrates (3000 rpm, 30 s, 1000 rpm). The substrates were subsequently annealed at 210 °C for 5 minutes. A layer of hole transport material (HTM) was spin-coated on top of the annealed films, which consisted of 78 mg of spiro-OMeTAD, 31 uL of 4-*tert*butylpyridine, 19 μL of bis(trifluoromethane) sulfonamide lithium salt (Li-TFSI) (517 mg mL^{-1} in acetonitrile) and 14 μL of FK209 Co^{3+} salt (376 mg mL^{-1} in acetonitrile). The spin-coating program was 4000 rpm, 40 s, 2000 rpm. Finally, a 80 nm thick Au layer was deposited by thermal evaporation.

2.3 Methods

XRD patterns were measured on a Brucker D2 X-Ray diffractometer with a copper X-ray tube (λ = 1.5418 Å, 300 W, 30 kV) as an X-ray generator and a Lynxeye (1D mode) detector. The measurements were conducted using a 2 theta range of 10°–40°, a step size of 0.04°, and a rate of 1 step per s. Fluorescence spectra were recorded with an Agilent Cary Eclipse spectrofluorometer, at a scan rate of 600 nm min^{-1}, in a 495–600 nm interval, manual voltage 550 V, with a bandwidth of excitation and emission slits at 5 nm for FS in the liquid phase and 2.5 nm for the solid phase. ^{1}H- and ^{13}C-NMR spectra were recorded on a Bruker Avance 400 MHz and a Bruker Avance 200 MHz. Purification of compounds 2 and 3 was carried out with Biotage Isolera ONE Flash Chromatography MPLC System. Purification of compound 5 was performed *via* Preparative HPLC purification on an Agilent Technologies 1260 Infinity preparative HPLC system using a Waters XSelect CSH Phenyl-Hexyl column (5 μm, 150 × 30 mm). The characterization of compound 5 was effectuated *via* Analytical HPLC analysis on an Agilent SERIES 1260 system on an XBridge® BEH C18 column (2.5 μm, 4.6 × 50 mm) and the mass spectra were recorded on a Thermo Finnigan (San Jose, CA, USA) UPLC system using a BEH Acquity UPLC column (1.7 μm, 2.1 × 50 mm^2) coupled with an LCQ ADV MAX ion-trap mass spectrometer (ESI† ion source). pH measurements were performed using a Crison Medidor PH BASIC 20 pH-Meter. ICP measurements were performed using a iCAP 7400 ICP-OES.

2.4 Spectroscopy analysis

To construct the calibration line, fluorescence measurements were carried out in the presence of increasing concentrations of PbI_2. Each analysis was made in triplicate and the calibration line was obtained from the average of the three different sets of experiments. The sensor stock solution was diluted in a final volume of 3 mL of 0.1 M PBS, at pH 4.5, to achieve a final concentration of 5.5 μM. An aqueous stock solution of PbI_2 153 μM was prepared with 10% HCl to facilitate dissolution of the salt. Sixteen solutions of FS 5.5 μM in PBS were prepared, with increasing concentrations of PbI_2, and the fluorescence spectrum was recorded for each addition. The experimental set was repeated three times with three different stock solutions of FS. PbI_2 detection of the standards solution was performed by calculating the Pb^{2+} concentration using the calibration line equation. For this analysis, we employed the same experimental conditions used to build the calibration line. To record fluorescence, 5 μL of a PbI_2 solution of known concentration was added to the FS solution in PBS. Each measurement was repeated three times. The same procedure was used to record the [PbI_2] of samples derived from PSCs. For fluorescence measurements on a solid substrate, 5 μL of PbI_2 5.5 mM stock solution were deposited on paper, and following FS adsorption,

2 μL of PbI_2 (HCl 10%) 760 μM solution was added. The experiment was carried out 3 times.

2.5 FS Synthesis

Compound 2 – *N*,*N*′-1,2-phenylenebis[*N*-(2-ethoxy-2-oxoethyl) glycine] 1,1′-diethyl ester. In a round-bottomed flask, 4.40 g (40.7 mmol) of 1,2-phenylendiamine, 5.10 g sodium iodide (34.0 mmol), 35 mL diisopropylethylamine (210.0 mmol) and 30 mL ethyl bromoacetate (270.0 mmol) were added and dissolved into 40 mL acetonitrile. The solution was refluxed for 16 h under argon, cooled to RT and diluted in water. The reaction mixture was extracted three times with 200 mL of dichloromethane. The organic phase was dried over sodium sulphate and dried under vacuum. The product was then purified by MPLC using cyclohexane/ethyl acetate (7 : 3, v/v) as an eluent, using a 100 g Biotage Sfar Silica D Cartridge with a 50 mL min^{-1} flow. The final product was recrystallized in 40 mL of ethanol to obtain 11.6 g (final yield 63%) of compound **2** as a white solid. ^{1}H NMR- (CDCl3, 300 MHz) δ 7.01–7.07 (m, 2H), 6.92–6.98 (m, 2H), 4.30 (s, 8H), 4.11 (q, J = 7.0 Hz, 8H), 1.19 (t, J = 7.0 Hz, 1H).

Compound 3 – *N*,*N*′-(4-formyl-1,2-phenylene)bis[*N*-(2-ethoxy-2-oxoethyl)glycine] 1,1′-diethyl ester. In a round-bottomed flask, 900 mg of compound 2 (2.0 mmol) was dissolved in 4 mL dry pyridine and 20 mL dry DMF (258.0 mmol). Under an argon atmosphere, the solution was cooled in an ice bath, then 15 mL of phosphorous oxychloride was added dropwise. The mixture was stirred for 1 h and then heated to 75 °C for 45 min. After reaction completion, the solution was cooled to RT, diluted with 50 mL of dichloromethane and 200 mL of water and ice mixture. Sodium carbonate was added to the mixture, and then it was extracted three times with 200 mL dichloromethane. The organic phase was dried over sodium sulfate and concentrated under vacuum to give a brown oil. The product was then purified by direct phase chromatography using cyclohexane/ethyl acetate (7 : 3, v/v) as an eluent to obtain 0.335 g (final yield 35%) of compound **3** as a yellow solid. ^{1}H NMR- ($CDCl_3$, 300 MHz) δ 9.81 (s, 1 H), 7.59 (s, 1H), 7.48 (d, J = 8 Hz, 1H), 7.10 (d, J = 8 Hz, 1H), 4.42 (s, 4H), 4.28 (s, 4H), 4.04–4.16 (m, 8H), 1.19 (t, J = 8 Hz,12H).

Compound 4 – (T-4)-[[1,1′-diethyl N,N′-[4-[(3,5-dimethyl-1*H*-pyrrol-2-yl-κN)(3,5-dimethyl-2*H*-pyrrol-2-ylidene-κN)methyl]-1,2-phenylene]bis[*N*-(2-ethoxy-2-oxoethyl)glycinato]](1-)]difluoroboron. In a one-necked flask, 580 mg of compound **3** (1.2 mmol), 0.32 mL of 2,4-dimethylpyrrole (3.6 mmol), 7 mL of dichloromethane and 2 drops of trifluoroacetic acid were added. The solution was stirred at RT and refluxed for 14 h under argon. In the same solution, 280 mg of 2,3-dichloro-5,6-dicyano-*p*-benzoquinone (1.3 mmol) were added, and the crude was stirred for other 4 h. Finally, 2.5 mL of triethylamine (18.0 mmol) and 2.5 mL of BF_3–OEt_2 were added and the reaction was stirred for a further 2 h. The mixture was diluted with 100 mL of water and extracted three times with 200 mL of dichloromethane. The organic phase was dried over sodium sulfate and concentrated under vacuum to give a purple oil. The product was then purified by direct phase flash chromatography using cyclohexane/ethyl acetate (7 : 3, v/v) as the eluent and dried to obtain 162.0 mg (18%) of compound 3 as an orange oil. ^{1}H NMR- ($CDCl_3$, 300 MHz) δ 7.13 (d, J = 8 Hz, 1H), 6.93 (s, 1H), 6.84 (d, J = 8 Hz, 1H), δ 5.95 (s, 2H), δ 4.35 (s, 4H), 4.29 (s, 4H), 4.02–4.17 (m, 8H), 2.55 (s, 6H), 1.40 (s, 6H), 1.16–1.27 (m, 12H).

Compound 5 (FS) (T-4)-[[2,2′,2″,2‴-[[4-[(3,5-dimethyl-1*H*-pyrrol-2-yl-κN)(3,5-dimethyl-2*H*-pyrrol-2-ylidene-κN)methyl]-1,2-phenylene]dinitrilo]tetrakis[*N*,*N*-bis(2-hydroxyethyl)acetamidato]](1-)]difluoroboron. In a one-necked flask, 135 mg of compound **4** (0.2 mmol), 22.3 g diethanolamine (212.1 mmol) were dissolved with 10 mL of acetonitrile. The solution was refluxed for 24 h under an argon atmosphere. After reaction competition, solvent was removed under vacuum. The final product was then purified by reverse phase column chromatography on a preparative HPLC using the method reported in Table SI6 (ESI†). After purification, the product was immediately neutralized with sodium carbonate to alkaline pH and dried. The resulting solid is then extracted with 2-propanol, filtered and dried to obtain 148.4 mg (final yield 83%) of compound **5** as a red solid. ^{1}H NMR- (D_2O, 400 MHz) δ 6.83 (brs, 1H), 6.73 (s, 1H), 6.33 (brs, 1H), 5.94 (s, 2H), 4.51 (s, 4H), 4.47 (s, 4H), 3.31–3.67 (m, 32H), 2.30 (s, 6H), 1.30 (s, 6H); ^{13}C NMR (400 MHz, D_2O) δ 172.7, 172.5, 155.3, 144.4, 142.6, 142.1, 141.9, 131.5, 127.5, 121.4, 121.3, 120.8, 117.9, 115.0, 112.1, 59.3, 59.2, 59.2, 59.1, 51.6, 51.4, 50.2, 50.0, 49.0, 48.7, 48.5, 13.9, 13.8.

3. Results and discussion

The fluorescent sensor (FS) was synthesized drawing from the synthetic protocol described by Lyu *et al.*, suitably optimized to adjust reaction times and improve purification steps in order to achieve higher yields.

The synthesis involves four steps (Scheme 1): in step A compound **1** is alkylated with ethyl bromoacetate to obtain compound **2** (final yield = 63%): the reaction time was increased from 7 h to 16 h, and the final product was purified through direct column chromatography (MPLC) using cyclohexane/ethyl acetate (7 : 3, v/v) as the eluent. Step B relies on the Vilsmeyer formylation reaction (yield = 35%) to introduce BODIPY chromophores by *in situ* condensation of compound 3 with 2, 4-dimethylpyrrole and insertion of BF_3–OEt_2 (yield = 18%). In steps B and C the products were purified by direct phase chromatography using cyclohexane/ethyl acetate (7 : 3, v/v) as the eluent. The final ester ammonolysis reaction of compound 4 with

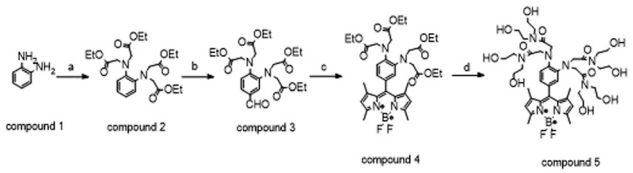

Scheme 1 (a) ethyl bromoacetate, KI, DIPEA, CH_3CN, reflux under Ar, 16 h, rt; (b) $POCl_3$, DMF, dry pyridine, reflux under Ar, rt, 1 h and warmed up to 75 °C, 45 min; (c) (1) 2,4-dimethylpyrrole-TFA, DCM, reflux under Ar, 14 h, rt; (2) DDQ, reflux under Ar, 4 h, rt; (3) NEt_3, BF_3·OEt_2, reflux under Ar, 2 h, rt; (d) diethanolamine, CH_3CN, reflux under Ar, 24 h, rt.

diethanolamine afforded the FS, which was purified by reverse-phase preparative HPLC with a final yield of 83%.

To verify the fluorescence enhancement of the sensor in the presence of Pb^{2+}, the quantum yields of the sensor and the sensor-Pb complex were calculated under the operating conditions ([FS] = 5.5 μM; PBS 0.1 M, pH = 4.5). Fluorescein in a 0.1 M NaOH solution was used as the standard, and it was observed that the Φ_{sensor} = 0.0104 ± 0.0002 and $\Phi_{complex}$ = 0.5370 ± 0.0025 values had increased compared to the work of Liu *et al.*, in which the quantum yields had been measured at pH 7.2. Furthermore, the influence of pH on the stoichiometry of the complex was investigated and a Job plot was constructed. Under neutral aqueous conditions with a pH of 7.2, the stoichiometry of the complex is FS : Pb^{2+} 1 : 2; however, under acidic pH conditions, the stoichiometry is FS : Pb^{2+} 1 : 1 (SI2, ESI†) due to the protonation of the nitrogen atoms in the side chains that do not have a lone pair available to complex the metal cation.

Finally, the possible competition of cations used in perovskite solar cells with Pb^{2+} and the influence of the counterion on lead complexation were investigated. The presence of other cations in solution does not change the sensor response, with two exceptions. The first is Ti^{4+} due to the fact that the salt used, titanium diisopropoxide bis(acetylacetonate), is commercially available in a 75% isopropanol solution. This can affect the pH of the sample and, therefore, reduce the sensor response. As for the counterion, the same response was observed for 2 equivalents of PbI_2 and $PbBr_2$, while the lower response for $PbCl_2$ was attributed to the salt's poor solubility in aqueous solution (SI3, ESI†). In order to prove the sensor efficiency in lead detection, several fluorescence analyses were performed. Initially, we used FS to create a calibration curve by fluorimetric titration. Since FS is sensitive to pH variations, all experiments were conducted in 0.1 M phosphate buffer solution (PBS) at pH 4.5 to mimic acidic rain conditions and to keep the experimental conditions constant. The calibration line, obtained from three replicates, shows the fluorescence response of the sensor as a function of Pb^{2+} concentration in the range of 0–2.3 μM. The sensor was employed in large excess [5.5 μM] over the analyte concentration to achieve the best possible linearity in the range of interest, which includes the legal limits for lead in drinking water. Fig. 2 shows the enhancement in fluorescence as the lead concentration increases. This confirms that complexation blocks the PET process by preventing chromophore quenching. The line fit with an R^2 = 0.9992 confirms the high linearity of the response and good reproducibility of the measurement. To confirm the sensitivity and accuracy of the calibration line, three aqueous standard solutions of PbI_2 were prepared and samples concentrations were measured by fluorimetric analysis. Each analysis was performed in triplicate and, as reported in Table 1, there was a good correlation between the standard effective concentration of PbI_2 and the value recorded through fluorescence analysis.

Finally, we tested our sensor to detect real perovskite byproducts, by immersing perovskite solar devices in rainwater.

For the experiment, we have employed two cells with different compositions: one organic–inorganic hybrid $FA_{0.8}MA_{0.2}PbI_3$ and one fully inorganic $CsPbI_3$, to evaluate the sensor behavior in the presence of organic and inorganic cations (Fig. 3(a)).

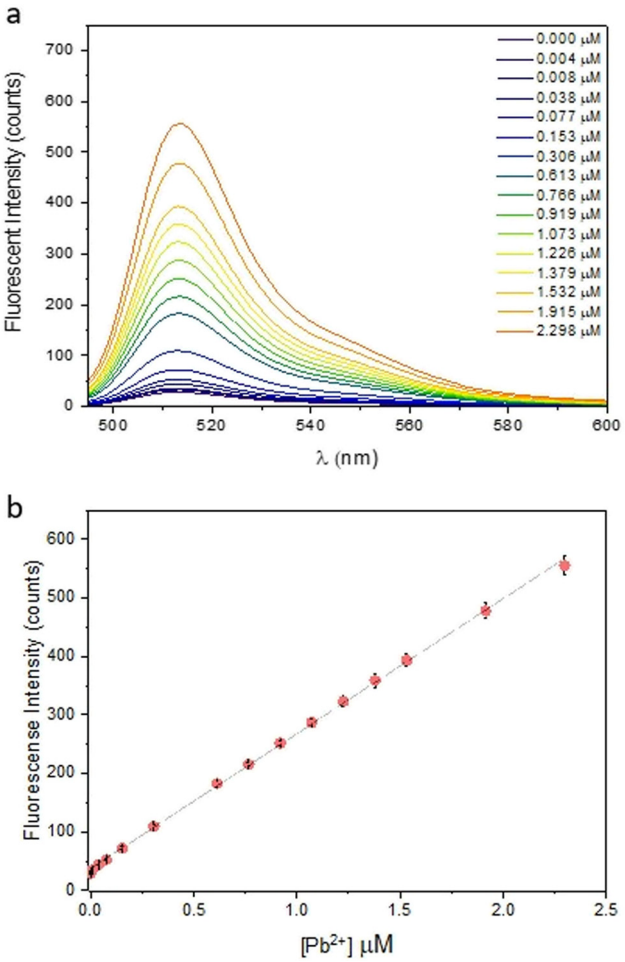

Fig. 2 (a) Fluorescence emission spectra (λ_{ex} = 470 nm) of FS (5.5 μM) in PBS buffer (0.1 M) pH 4.5 with different concentration of Pb^{2+} (0–2.3 μM); (b) fluorescent intensity at 512 nm as a function of [Pb^{2+}].

To validate the results from the degraded cells, we also prepared a stand-alone perovskite film of $FA_{0.8}MA_{0.2}PbI_3$ (therefore, without transport layers or gold terminal) to assess the presence of interferents arising from the layers of the cell.

The results of our analysis for both the solar cells and the stand-alone film are cross-checked with the elemental quantification obtained by ICP-OES and presented in Table 2. The experiments confirmed the release of PbI_2 from all three different samples, with the maximum value of 1617.68 μg l^{-1}, detected for the FAMA perovskite film, while lower values were observed for the samples derived from the cells. The reduced standard deviations also confirm good experimental reproducibility. We found a good agreement between ICP and fluorescence analysis

Table 1 Quantification of PbI_2 present in the standard solutions. Measurements performed with [FS] 5.5 μM, in PBS (0.1 M) pH 4.5

	Effective conc. (mg L^{-1})	Experimental conc. (mg L^{-1})	Err.%
Std 1	279.00	278.24 ± 3.18	0.27
Std 2	166.60	167.36 ± 3.55	0.45
Std 3	350.60	349.78 ± 2.25	0.23

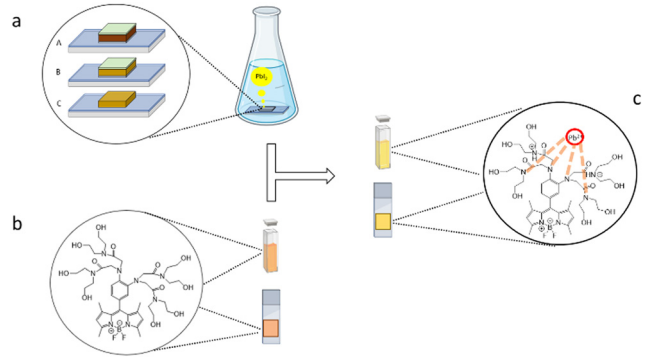

Fig. 3 schematic representation of Pb^{2+} release mechanism from PSCs: (A) $CsPbI_3$; (B) PSCs of $FA_{0.8}MA_{0.2}PbI_3$; (C) $FA_{0.8}MA_{0.2}PbI_3$ perovskite film (a); sensor in liquid phase and supported on solid substrate for fluorimetric measurements (b); and sensor complexation and fluorescence enhancement (c).

Table 2 Quantification of PbI_2 present in the PSCs after soaking in rainwater. Measurements made with [FS] 5.5 μM, in PBS (0.1 M) pH 4.5

	ICP μg l^{-1}	Fluor. μg l^{-1}	Err. %
$CsPbI_3$ PSC	620.00	610.37 ± 2.02	1.55
$FA_{0.8}MA_{0.2}PbI_3$ PSC	326.00	384.77 ± 2.48	18.03
$FA_{0.8}MA_{0.2}PbI_3$ perovskite film	1633.00	1617.68 ± 7.74	0.94

Table 3 Fluorescence intensity (F.I.) expressed in counts of three FS samples supported by a solid phase in the absence and presence of the cation Pb^{2+}

	F.I. sensor	F.I. sensor + Pb^{2+}	F.I. enhancement
Sample 1	253.93	331.71	30.63%
Sample 2	242.33	344.70	42.24%
Sample 3	214.52	341.00	58.96%

for the $CsPbI_3$ PSC cell, while for the $FA_{0.8}MA_{0.2}PbI_3$ cell a slight overestimation of [PbI_2] was observed, despite very similar results recorded with the two different analytical techniques.

In addition, we have investigated the behavior of FS when supported by a solid substrate (Fig. 3(c)). To this aim, 5 μL of 5.5 mM FS sensor stock solution was deposited on paper and the fluorescence spectrum was recorded. Then, 2 μL of PbI_2 760 μM standard solution was added to check the fluorescence enhancement. In Table 3 we showed that in all samples the fluorescence intensity increases between 31% and 59%, confirming that FS can also act as an on–off sensor on a solid support and not only in solution.

4. Conclusions

In this work, we explored the possibility of detecting and quantifying Pb^{2+} released from PSCs promoted by rain. The calibration curve was calculated at pH 4.5, in the range of [Pb^{2+}] including the legal limits imposed by the world's leading organizations on heavy metal contamination in drinking water. The concentrations of PbI_2 released from the PSC cells were then quantified, and the results obtained for the $CsPbI_3$ cell and the perovskite were in agreement with ICP data, while an error % of 18% was found for the PSC $FA_{0.8}MA_{0.2}PbI_3$. In addition, the possibility of using the FS as an on–off sensor supported by a solid phase was investigated. The fluorescence enhancement observed for the samples confirmed this possible new application. The results obtained are encouraging and the sensor may be applied in the industrial field as a control for lead release in PSC fabrication processes. In the future, it will be necessary to verify the behavior of the sensor with PSCs of different architectures and processes. The further possible application involves the field of photovoltaic panels, with the possibility of verifying through simple fluorimetric experiments water pollution near photovoltaic installations.

Conflicts of interest

There are no conflicts to declare.

Acknowledgements

The authors acknowledge prof. Antonella Profumo for the ICP-OES analysis, the "HY-NANO" project that received funding from the European Research Council (ERC) Starting Grant 2018 under the European Union's Horizon 2020 research and innovation program (grant agreement no. 802862) and the Fondazione Cariplo conomia Circolare 2021 Project "Green flexible hybrid perovskite solar module for the market: from smart lead manipulation to recycling" (FLHYPER,no 20201067), funded under the "Circular Economy-2020"call. R. M. and G. G. acknowledge the PhD Fellowship from Eni S.p.A. The authors acknowledge the support from the Ministero dell'Università e della Ricerca (MUR) and the University of Pavia through the program "Dipartimenti di Eccellenza 2023–2027".

Notes and references

1 Y. Yao, M. Wang, Q. Cai and D. Wei, *Nanoscale*, 2022, **14**, 7203–7210.
2 K. Yoshikawa, H. Kawasaki, W. Yoshida, T. Irie, K. Konishi, K. Nakano, T. Uto, D. Adachi, M. Kanematsu, H. Uzu and K. Yamamoto, *Nat. Energy*, 2017, **2**, 1–8.
3 S. De Wolf, J. Holovsky, S.-J. Moon, P. Löper, B. Niesen, M. Ledinsky, F.-J. Haug, J.-H. Yum and C. Ballif, *J. Phys. Chem. Lett.*, 2014, **5**, 1035–1039.
4 S. D. Stranks, G. E. Eperon, G. Grancini, C. Menelaou, M. J. P. Alcocer, T. Leijtens, L. M. Herz, A. Petrozza and H. J. Snaith, *Science*, 2013, **342**, 341–344.
5 V. D'Innocenzo, A. R. Srimath Kandada, M. De Bastiani, M. Gandini and A. Petrozza, *J. Am. Chem. Soc.*, 2014, **136**, 17730–17733.
6 Y. Zhao, F. Ma, Z. Qu, S. Yu, T. Shen, H.-X. Deng, X. Chu, X. Peng, Y. Yuan, X. Zhang and J. You, *Science*, 2022, **377**, 531–534.
7 R. Azmi, E. Ugur, A. Seitkhan, F. Aljamaan, A. S. Subbiah, J. Liu, G. T. Harrison, M. I. Nugraha, M. K. Eswaran,

M. Babics, Y. Chen, F. Xu, T. G. Allen, A. ur Rehman, C.-L. Wang, T. D. Anthopoulos, U. Schwingenschlögl, M. De Bastiani, E. Aydin and S. De Wolf, *Science*, 2022, **376**, 73–77.
8 G. Divitini, S. Cacovich, F. Matteocci, L. Cinà, A. Di Carlo and C. Ducati, *Nat. Energy*, 2016, **1**, 1–6.
9 S. Kundu and T. L. Kelly, *EcoMat*, 2020, **2**, e12025.
10 N. Aristidou, C. Eames, I. Sanchez-Molina, X. Bu, J. Kosco, M. S. Islam and S. A. Haque, *Nat. Commun.*, 2017, **8**, 15218.
11 T. Leijtens, G. E. Eperon, N. K. Noel, S. N. Habisreutinger, A. Petrozza and H. J. Snaith, *Adv. Energy Mater.*, 2015, **5**, 1500963.
12 J. Yang, B. D. Siempelkamp, D. Liu and T. L. Kelly, *ACS Nano*, 2015, **9**, 1955–1963.
13 L. Shi, M. P. Bucknall, T. L. Young, M. Zhang, L. Hu, J. Bing, D. S. Lee, J. Kim, T. Wu, N. Takamure, D. R. McKenzie, S. Huang, M. A. Green and A. W. Y. Ho-Baillie, *Science*, 2020, **368**, eaba2412.
14 G. Schileo and G. Grancini, *J. Phys. Energy*, 2020, **2**, 021005.
15 A. L. Wani, A. Ara and J. A. Usmani, *Interdiscip. Toxicol.*, 2015, **8**, 55–64.
16 I. Turkevych, S. Kazaoui, E. Ito, T. Urano, K. Yamada, H. Tomiyasu, H. Yamagishi, M. Kondo and S. Aramaki, *ChemSusChem*, 2017, **10**, 3754–3759.
17 A. Aftab and Md. I. Ahmad, *Sol. Energy*, 2021, **216**, 26–47.
18 J. Cao and F. Yan, *Energy Environ. Sci.*, 2021, **14**, 1286–1325.
19 R. Lin, K. Xiao, Z. Qin, Q. Han, C. Zhang, M. Wei, M. I. Saidaminov, Y. Gao, J. Xu, M. Xiao, A. Li, J. Zhu, E. H. Sargent and H. Tan, *Nat. Energy*, 2019, **4**, 864–873.
20 K. Xiao, R. Lin, Q. Han, Y. Hou, Z. Qin, H. T. Nguyen, J. Wen, M. Wei, V. Yeddu, M. I. Saidaminov, Y. Gao, X. Luo, Y. Wang, H. Gao, C. Zhang, J. Xu, J. Zhu, E. H. Sargent and H. Tan, *Nat. Energy*, 2020, **5**, 870–880.
21 R. Lin, J. Xu, M. Wei, Y. Wang, Z. Qin, Z. Liu, J. Wu, K. Xiao, B. Chen, S. M. Park, G. Chen, H. R. Atapattu, K. R. Graham, J. Xu, J. Zhu, L. Li, C. Zhang, E. H. Sargent and H. Tan, *Nature*, 2022, **603**, 73–78.
22 C. Ponti, G. Nasti, D. Di Girolamo, I. Cantone, F. A. Alharthi and A. Abate, *Trends Ecol. Evol.*, 2022, **37**, 281–283.
23 J. Li, H.-L. Cao, W.-B. Jiao, Q. Wang, M. Wei, I. Cantone, J. Lü and A. Abate, *Nat. Commun.*, 2020, **11**, 310.
24 K. Dedecker and G. Grancini, *Adv. Energy Mater.*, 2020, **10**, 2001471.
25 Y. G. Yoo, J. Park, H. N. Umh, S. Y. Lee, S. Bae, Y. H. Kim, S. E. Jerng, Y. Kim and J. Yi, *J. Ind. Eng. Chem.*, 2019, **70**, 453–461.
26 J. Liu, K. Wu, S. Li, T. Song, Y. Han and X. Li, *Dalton Trans.*, 2013, **42**, 3854–3859.
27 H. Guo, Z. Zheng, Y. Zhang, H. Lin and Q. Xu, *Sens. Actuators, B*, 2017, **248**, 430–436.
28 H. M. Marwani, J. Ahmed and M. M. Rahman, *Sensors*, 2022, **22**, 8976.
29 S. V. Smirnova, D. V. Ilin and I. V. Pletnev, *Talanta*, 2021, **221**, 121485.
30 Y. Song, F. Guo, P. Zeng, J. Liu, Y. Wang and H. Cheng, *Anal. Chim. Acta*, 2022, **1212**, 339935.
31 Y. Yu, S. S. Naik, Y. Oh, J. Theerthagiri, S. J. Lee and M. Y. Choi, *J. Hazard. Mater.*, 2021, **420**, 126585.
32 M. Aamir, M. Sher, M. Azad Malik, J. Akhtar and N. Revaprasadu, *New J. Chem.*, 2016, **40**, 9719–9724.
33 C. Tsaridou and A. J. Karabelas, *Water*, 2021, **13**, 2918.
34 EUR-Lex – 32020L2184 – EN – EUR-Lex, **https://eur-lex.europa.eu/eli/dir/2020/2184/oj**, (accessed August 11, 2022).